Additive Manufacturing Letters 7 (2023) 100182

Contents lists available at ScienceDirect

Additive Manufacturing Letters

journal homepage: www.elsevier.com/locate/addlet

Short Communication

Effect of layer thickness, and laser energy density on the recrystallization behavior of additively manufactured Hastelloy X by laser powder bed fusion

Faraz Deirmina [a,1], Olutayo Adegoke [a], Matteo Del Col [b], Massimo Pellizzari [b,*]

[a] Siemens Energy AB, Finspång, Sweden
[b] Department of Industrial Engineering, University of Trento, Via Sommarive 9, Trento 38123, Italy

ARTICLE INFO

Key words:
Ni-superalloy
L-PBF, EBSD
Laser energy density
Recrystallization

ABSTRACT

A single-phase Ni-superalloy (Hastelloy X) was fabricated by laser powder bed fusion (L-PBF) using different layer-thicknesses (i.e., 40, 60, 80, and 120 μm), by implementing different optimized volumetric laser energy densities (i.e., VED of 67, 44, 31, and 35 J/mm^3). As-built (AB) microstructure, grain morphology, and the recrystallization kinetics were systematically dependent on VED which generally decreases by increasing layer thickness. An increased VED led to a columnar grain morphology, strong texture, large lattice micro-strain, high fraction of low angle boundaries, and increased yield strength. Electron back scattered diffraction (EBSD) analysis revealed that also the recrystallization kinetics was significantly dependent on VED. By decreasing the VED, recrystallization was largely suppressed because of the lower dislocation density in the AB state. A processing map to study the recrystallization as a function of VED, and solution annealing temperature is proposed.

Introduction

Hastelloy X (HX) is a nickel-chromium-iron-molybdenum single-phase austenitic superalloy well known for its high-temperature strength, and oxidation resistance [1–3]. Thanks to its good weldability, HX is also one of the most exploited commercial superalloys for additive manufacturing (AM) [4]. The design freedom offered by AM, enables engineering and manufacturing of cooling channels with improved cooling efficiency for the use in gas-turbine engines, combustor parts, burners, exhaust-end components, transition pieces, and high-temperature gas cooled reactors [1–3]. The most practiced AM processing route for Ni superalloys such as HX is laser powder bed fusion (L-PBF) which enables achieving near full dense components with the possibility of manufacturing near-surface intricate cooling channels with high resolution, and relatively low surface roughness [5].

From a metallurgical viewpoint, the peculiar microstructure achieved by laser powder bed fusion (L-PBF) is different from that of wrought counterpart, particularly due to the high anisotropy. The grain morphology, along the building direction (BD), is normally columnar and highly textured. The microstructure comprises a cellular/dendritic solidification structure as a result of high constitutional undercooling, with the micro-segregation of alloying elements to the cell boundaries because of rapid solidification [6,7]. In some cases, these features have to be removed by a subsequent homogenization or solution annealing treatment, especially when anisotropy in mechanical properties, with respect to the BD, and fine grain sizes (e.g., reduced creep life) are of concern [7–9]. Li et al. [10] showed that by a high temperature solution annealing, the tensile strength and dislocation density of HX fabricated by L-PBF was decreased while elongation was improved significantly with an evident increase in the grain size through full recrystallization and subsequent grain growth. Kangazian et al. [11] argued that in their honeycomb structures processed by a 30 μm layer thickness, solution annealing at 1175 °C for 2 h led to a partial recrystallization through a twining induced nucleation mechanism, while the recrystallized grains retained the texture from the prior (parent) grains slowing down the kinetics of recrystallization due to creation of low mobility boundaries.

With the technological advancements in L-PBF equipment, capable of providing larger laser powers, printing with larger powder-bed layer thicknesses aimed at increasing the productivity is now possible [12–14]. For instance, Schwerz et al. [15] showed by optimizing processing parameters, and utilizing the optimum build area, and increasing the layer thickness up to 150 μm, the productivity increased

* Corresponding author.
E-mail address: massimo.pellizzari@unitn.it (M. Pellizzari).
[1] Faraz Deirmina is now with Sandvik AB, Sweden

https://doi.org/10.1016/j.addlet.2023.100182
Received 13 September 2023; Received in revised form 15 October 2023; Accepted 16 October 2023
Available online 19 October 2023

Table 1
L-PBF parameters, density, and heat treatment of samples.

Layer thickness [μm]	Volumetric energy density (VED) [J/mm^3]	Sample code	Rel. Density (%)	Solution annealing temperatures, 2 h [°C]
40	~67	40 μm	≥99.5	1150, 1175, 1200, 1250
60	~44	60 μm	≥99.5	1150, 1175, 1200, 1250
80	~31	80 μm	≥99.5	1150, 1175, 1200, 1250
120	~35	120 μm	≥99.5	1150, 1175, 1200, 1250

by a factor of 4 to 10 for L-PBF HX. However, as shown in references [12–15], the change in the effective heat input related to the increased layer thickness (i.e., volume of the powder bed to be melted), and consequently the laser energy density, might change the thermal history leading to the development of different grain morphologies, microstructures, and defects density (e.g., dislocation density). This might eventually change the response of the material to heat treatment. To the authors best knowledge, the response to heat treatment for larger layer thickness production of L-PBF components is still not widely elaborated.

In this communication, the authors studied the influence of the as built (AB) microstructure obtained by modifying the layer thickness, and laser energy density, on the recrystallization behavior of the L-PBF HX.

Materials and methods

Argon atomized HX powders with a nominal chemical composition of 21.00 Cr, 18.00 Fe, 8.50 Mo, 1.50 Co, 0.70 W, 0.15 Si, 0.02 C, and Ni bal. in wt.% were used as feedstock material. The samples were processed by an EOS M290 equipment using four different layer thicknesses (i.e., 40, 60, 80, and 120 μm). They were then subjected to solution annealing for 2 h at four different temperatures (i.e., 1150 °C, 1175 °C, 1200 °C, and 1250 °C). Table 1 summarizes the list of the samples investigated and the corresponding optimized volumetric energy density (VED) (Eq. (1)), used for each layer thickness.

$$\mathrm{VED} = \frac{P}{v.h.t} \quad (1)$$

where P is the laser power (J/s), v is the scan speed (mm/s), t is the layer thickness (mm), and h is the hatch spacing (mm). Unfortunately, it is not possible to disclose the laser power, scanning speed and hatch spacing used for the higher layer thicknesses, however, authors confirm that the laser power gradually increased from 285 W (40 μm), by increasing the layer thickness, while the scanning speed and hatch spacing slightly decreased by increasing the layer thickness. However, it is evident that by increasing the layer thickness (t), the resulting VED generally, and inevitably becomes smaller. The only exception was in the 120 μm, where employing significantly higher power, and smaller hatch spacing, lead to a larger VED than that of 80 μm. Light optical microscopy (LOM) images of samples are included in supplementary file 1.

Solution annealing was carried out in a chamber furnace, followed by water quenching from the soaking temperature. The microstructure was studied by field emission scanning electron microscopy (FE-SEM), on the ground (up to 1200 grit), and polished (diamond paste 3 μm and 1 μm, colloidal silica, 0.02 μm) metallographic cross-sections. SEM imaging was performed using an accelerating voltage of 10 kV. Electron backscattered diffraction (EBSD) was carried out using a Symmetry EBSD detector on FE-SEM. A 20 kV accelerating voltage was used for the EBSD analysis, the magnification was set to 250X, with a step size of 2 μm. The post processing of data was carried out using Channel 5 suite (Tango mapping). For the geometrically necessary dislocations (GNDs) density measurements using EBSD results, the procedure in the work of Calcagnotto et.al. [16] was followed. X-Ray Diffraction (XRD) analysis carried out using an Italstructures (IPD3000/CPS120) instrument equipped with Co K_α source of 2000 W ($\lambda = 0.17889$ nm). The tilting angle of the specimen was set as $\Omega = 6°$ The diffraction spectra were analyzed by Rietveld method using MAUD software (Materials Analysis Using Diffraction) [17]. Vickers Hardness (HV10) measurements were performed according to ASTM E92. Tensile tests at room temperature

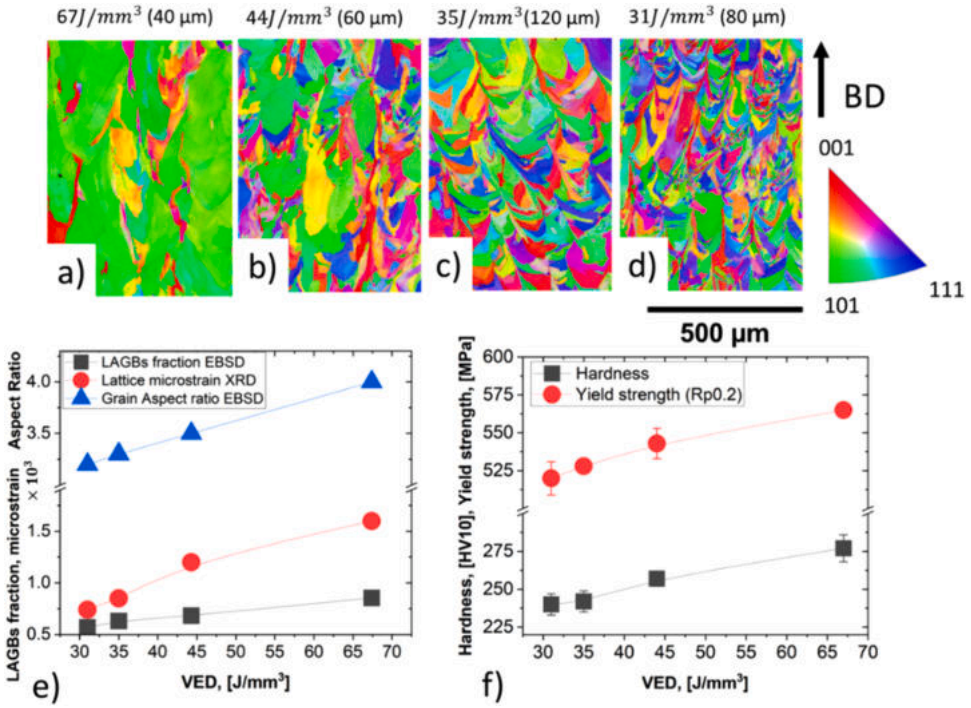

Fig. 1. IPF-Y maps of the AB samples, (a) 40 μm (67 J/mm^3), (b) 60 μm (44 J/mm^3), (c) 120 μm (35 J/mm^3), (d) 80 μm (31 J/mm^3), (e) Lattice mean micro-strain, LAGBs frequency, and grain aspect ratio vs. VED, and f) AB hardness, and yield strength vs. VED.

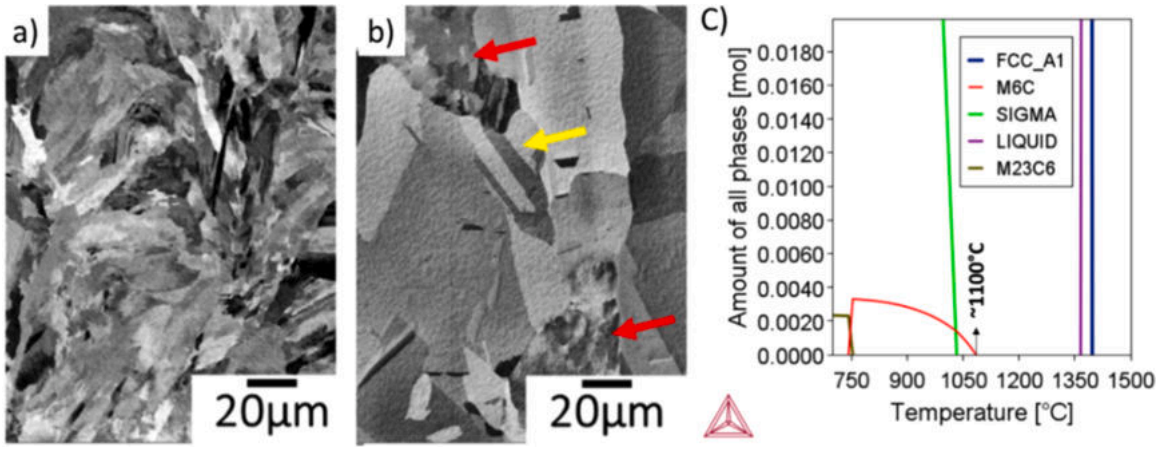

Fig. 2. SEM micrographs of (a) AB condition, (b) solution annealed, and (c) Equilibrium step diagram.

were carried out using cylindrical test blanks with main axis along the building direction (11.5 mm in diameter, and 80 mm in length) machined to the dimensions conforming to EN ISO 6892–1. Thermodynamic simulations were carried out using Thermo-Calc software (TTNi database v.8.3) [18]

Results

As built microstructures

Looking at the inverse pole Fig (IPF-Y) maps (along BD), the AB 40 µm shows a columnar grain morphology with a strong texture along <101>// BD (Fig 1a). The texture becomes weaker in the AB 60 µm, while a columnar grain microstructure still prevails (Fig. 1b). In 80 µm, and 120 µm samples, the microstructure shows a transition from columnar to a more equiaxed grain structure (Fig. 1c, and d). By increasing the layer thickness and inevitability decreasing the VED (see Table 1), the texture intensity decreased, and a more randomly textured polycrystalline microstructure could be obtained, as reported by Gokcekaya et al. [19] for Inconel 718 fabricated by L-PBF, and by Leicht et al. [12]. for AISI 316 L stainless austenitic steel. This transition is explained by the degree of constitutional supercooling, determined by the G/R ratio, where G is the thermal gradient, and R is the migration velocity of the solid-liquid interface. When the G/R ratio decreases, the solidification microstructure shows a transition from columnar dendritic towards equiaxed dendritic [19]. At a constant layer thickness, R increases by decreasing the laser power or increasing the scan speed, i.e., by reducing the heat input given to a certain volume of powders. In this study, by increasing the layer thickness, volumetric energy density as a simple, yet not precise, measure for the normalized heat input is decreased. Lower VED (less normalized heat input) most probably corresponds to higher R and reduced thermal gradient. Indeed, by the aid of modeling and experimental analysis, Hyer and Petrie [20] showed that the cooling rate increases by increasing the layer thickness in laser powder bed fusion processing of AISI 316 L. This leads to a transition from highly columnar to nearly equiaxed microstructure. In simple words, using smaller layer thickness or increased VED, a larger volume of the already solidified layers will be subjected to remelting upon deposition of the new layer, this leads to a stronger texture (<101>// BD) and columnar morphology due to the stronger competitive growth occurring preferentially along the easy-growth direction (i.e., along building direction) as a result of increased energy input [15]. This was also evident in the grain aspect ratio measurements along the BD in this work manifesting that by decreasing the VED, grain aspect ratio decreases gradually from over 4.0 (VED of 67 J/mm^3) to 2.9 (VED of 31 J/mm^3) (Fig. 1e).

The misorientation angle distribution measured using EBSD shows a larger frequency of low angle boundaries (LAGBs) (i.e., < 15° misorientation) when larger VED is used (Fig. 1e). This confirms a larger dislocation density by increasing the process heat input. This is backed with the lattice mean micro-strain calculated using XRD analysis, showing a gradual increase by increasing the VED (Fig. 1e). The minimum micro-strain was recorded for 80 µm sample (i.e., 0.00075) and the maximum was found in 40 µm specimen (i.e., 0.00160). The latter lies in the range of a severely deformed wrought HX, while the former is ~2 times that of wrought un-treated material [21]. Accordingly, the hardness (i.e., 240±7, 242±7, 257±5, and 277±9 HV10), and yield strength (i.e., 520±11, 528±1, 543±10, and 565±5 MPa) in AB condition increased by increasing the VED (Fig. 1f). Leicht et al. [12] observed similar drop in yield strength of L-PBF processed AISI 316 L, where the samples processed by 80 µm layer thickness and inevitably lower VED of ~40 J/mm^3 showed a yield strength of 460 MPa, while those of 20 µm layer thickness (VED of ~90 J/mm^3) had a yield strength of 540 MPa. They also confirmed the larger dislocation density in parts processed by lower layer thickness and higher VED.

Looking at the trends in Fig. 1, dislocation density, yield strength, and hardness are directly correlated to the VED, and not to the layer thickness. This is evident when comparing 80 µm, and 120 µm samples. The VED used for the 120 µm was larger than that of 80 µm, and consequently lattice micro-strain, LAGBs fraction, hardness, and yield strength were larger than those of 80 µm. It must be noted that the mean grain size, considering grain boundaries with larger than 15° misorientation, was 60±43, 55±39, 55±18, and 50±15 µm for 40, 60, 120, and 80 µm samples respectively. This would exclude Hall-Petch strengthening contribution differences in the samples, therefore, the increase in yield strength could be majorly related to dislocation density difference. Moreover, the standard deviation seems to decrease in equiaxed grain microstructure compared to samples showing columnar grain morphology.

Recrystallization behavior

An example of the microstrucure before and after the solution annealing process is presented in Fig. 2. The AB material shows highly strained grains with internal grain rotations (Fig. 2a), while the solution annealed microstructure consists of strain free recrystallized grains, annealing twins (yellow arrow), and retained highly strained grain clusters which are not yet recrystallized (red arrows), and seemingly are being consumed by the growth of the neighboring grains (Fig. 2b). All the solution annealing temperatures (Table 1), were above the solvus temperature of the intermetallic phases and carbides (i.e., ~1100 °C), as calculated with Thermo-Calc using the chemical composition of the starting powders (Fig. 2c). Therefore, any mechanism involving pinning of the grain boundaries by the precipitates could be neglected, and the

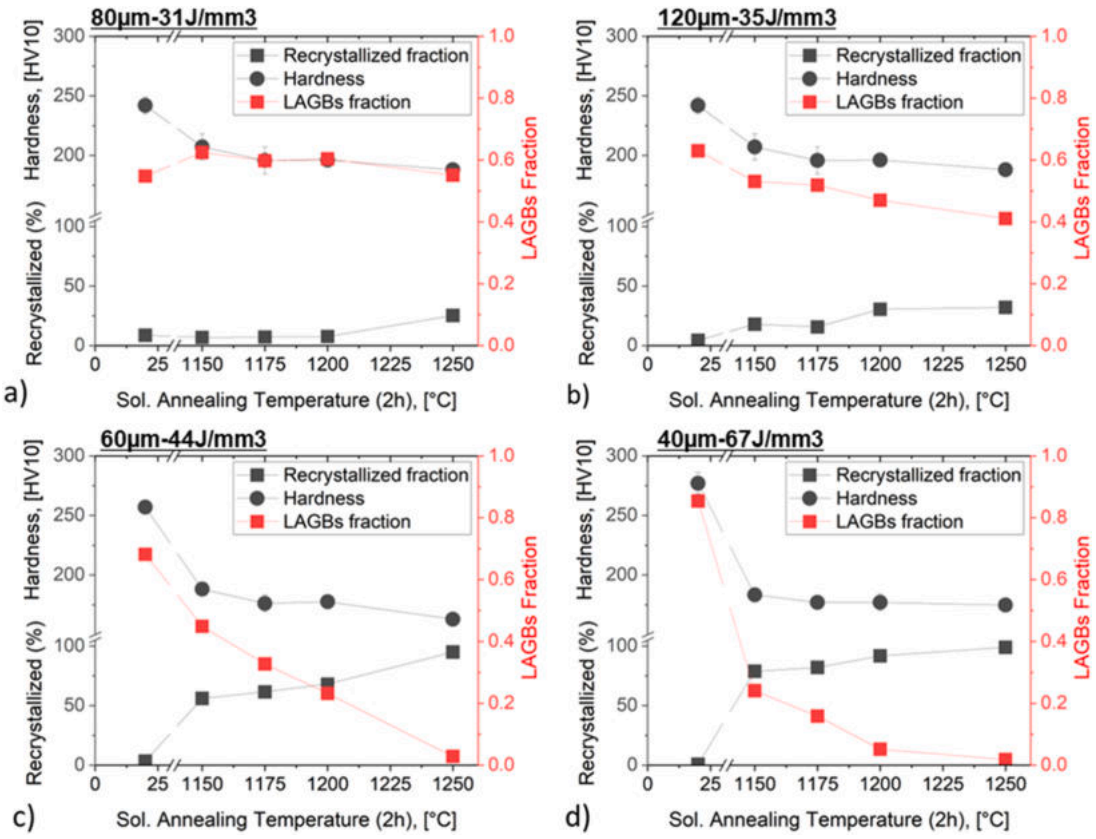

Fig. 3. a) Recrystallized fraction, hardness, and LAGBs fraction at different solution annealing temperatures, (a) 80 µm, (b) 120 µm, (c) 60 µm, and (d) 40 µm.

driving force for static recrystallization should be regarded as that of a single phase austenitic alloy.

Data extracted from the EBSD scans of the AB, and solution annealed samples are plotted in Fig. 3, and the corresponding EBSD reconstructed maps are shown in Fig. 4. The microstructure of AB 80 µm sample produced with the lowest VED, showing the lowest LAGBs fraction (i.e., ~0.55) exhibited ~8.0 vol.% strain free, in situ recrystallized grains (Figs. 3a, and 4, in blue) [22,23]. The AB microstructure was not affected by the heat treatment up to 1200 °C, characterized by unchanged recrystallized fraction and LAGBs frequency, and a slight drop in hardness, caused by partial recovery compared with the AB condition (i.e., 240 HV10 vs. ~200 HV10). At 1250 °C, partial recrystallization and emergence of the isolated recrystallized regions was evident. In these strain free grains, annealing twins were generated (Fig. 4, in white). The recrystallized fraction increased to around 25 % and slight decrease in LAGBs, and hardness (i.e., 195 HV10) was evident (Fig. 3a).

As shown in Figs. 3b, and 4, 120 µm sample with a VED of 35 J/mm^3, and initial LAGBs fraction of ~0.63 comprised around 4.5 vol.% of isolated strain free grains. By solution annealing, an enhanced recrystallization kinetics was evident compared with 80 µm, where at 1175 °C, ~15 % of the microstructure was recrystallized and LAGBs fraction decreased to ~0.5. The recrystallized fraction progressively increased by increasing the solution annealing temperature, and at 1250 °C, over 30 % of recrystallization took place. Accordingly, a reduction of LAGBs fraction to ~0.4, and hardness (i.e.,188 vs. 242 HV10) were observed.

60 µm sample processed using a VED of ~44 J/mm^3, with a starting LAGBs fraction of ~0.7, showed significantly enhanced recrystallization response (Figs. 3c and 4). In AB condition 3.5 vol.% of the grains were already strain free. At the lowest annealing temperature (i.e., 1150 °C), the material reached ~55 % recrystallization and LAGBs fraction was reduced to ~0.45. Solution annealing at 1175 °C, and 1200 °C resulted in ~62, and 70 % recrystallization, respectively, with a gradual reduction in LAGBs fraction (i.e., 0.32, and 0.23, respectively). At 1250 °C, the microstructure was nearly fully recrystallized (i.e., > 95 %). This was accompanied by a significant grain growth (see Fig. 4). Consequently, the fraction of LAGBs approached to nearly zero (i.e., 0.03) (Figs. 3c, and 4). In line with recrystallization evolution a gradual drop in hardness was evident reaching a final value of ~163 HV10.

The response to recrystallization further increased for the 40 µm sample produced with the highest VED (i.e., ~67 J/mm^3), showing the highest LAGBs fraction, (0.85). AB material comprised less than 1 % strain free grains. At 1150 °C, already ~80 % recrystallization was complete, agreeing with a sudden drop in LAGBs fraction (i.e., ~0.85 to 0.2), and hardness (i.e., 277 to 183 HV10). At 1200 °C, a nearly full recrystallization (> 90 %) was achieved, and the LAGBs fraction was only ~0.05. At 1250 °C, grain growth was evident, the LAGBs fraction was further reduced to ~0.02 while the recrystallization was almost complete, and hardness was ~175 HV10 (Figs. 3d and 4).

It was shown that the vol.% of strain free grains in AB condition increased by decreasing the VED. According to Eskandari sabzi et al. [22] the presence of strain free grains in AB state is a result of in situ recrystallization due to the multiple thermal cycles each layer experiences in solid state during the building process. It is plausible that in case of lower VED, and higher layer thicknesses were remelting of the already solidified layers is less pronounced, the thermal condition for in situ annealing of the solidified material was met, leading to an enhanced local recovery and partial recrystallization.

In all cases, the recrystallized grains comprise a large density of twin boundaries, given the increase in recrystallized fraction and twin boundaries intensity by increasing the annealing temperature, the recrystallization mechanism maybe be considered as twinning and recovery assisted recrystallization in this single-phase austenitic material. This agrees with the observations of Kangazian et al. [11]. Indeed, microstructures with highly stored energy (e.g., the case of L-PBF microstructure) favor the generation of annealing twins during recrystallization [24] supporting the retardation of recrystallization in

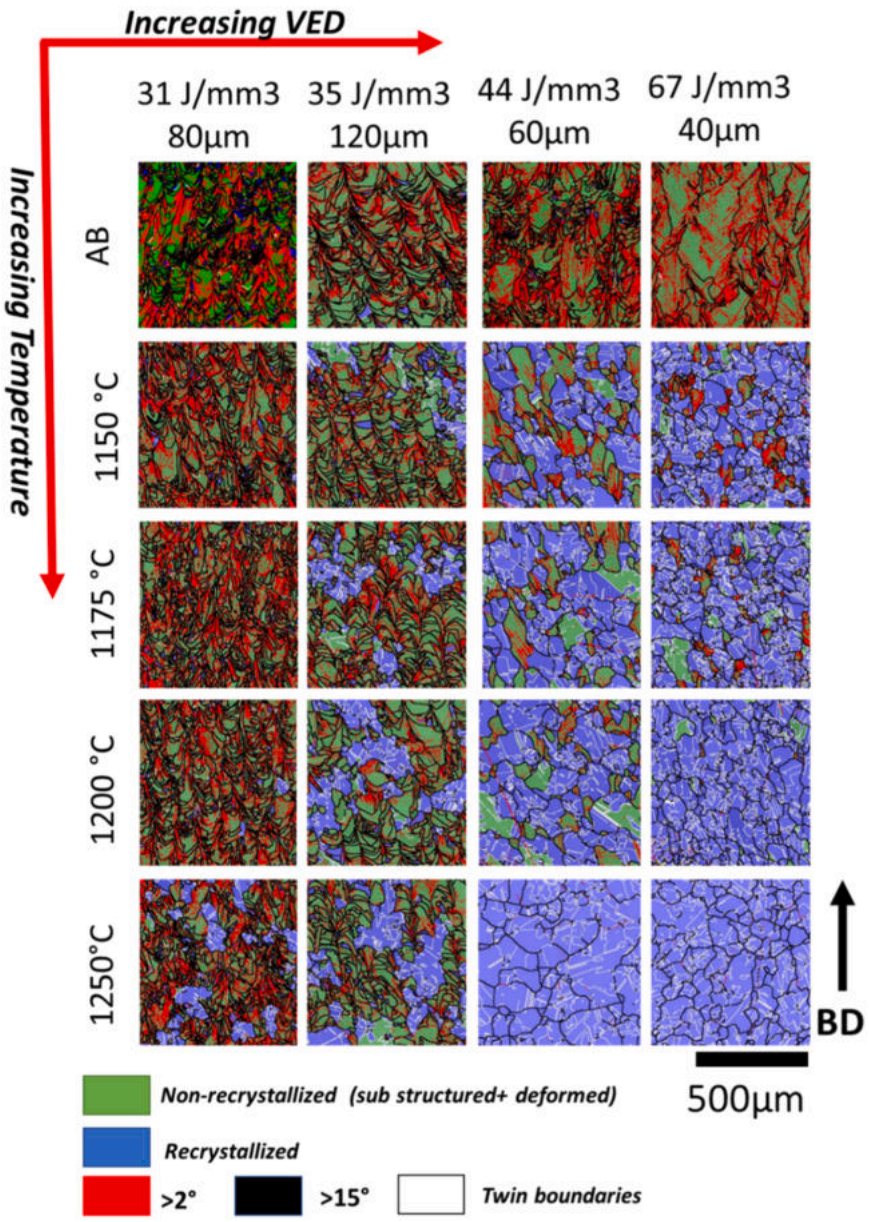

Fig. 4. EBSD processed maps for the samples with a focus on recrystallization behavior.

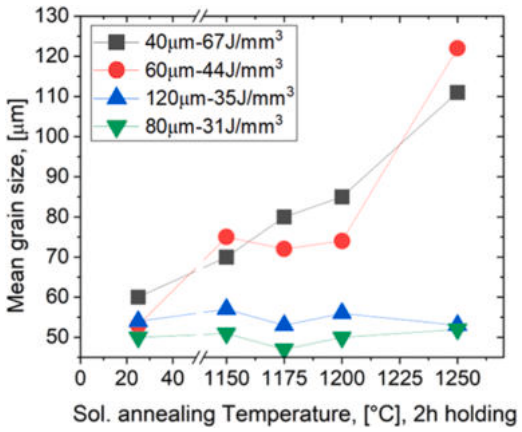

Fig. 5. Mean grain size vs. solution annealing temperature.

materials with lower stored energy (e.g., lower dislocation density).

With regards to grain size, it was observed that the grain sizes of 80 and 120 µm samples was not changed significantly by increasing the solution annealing temperature, in agreement with their poor recrystallization behavior. On the contrary both 40 µm, and 60 µm showed an increase in grain size (i.e., from 60 and 55 µm respectively, to ~70 µm) already at 1150 °C where both samples showed quite significant recrystallization. The trend remained almost steady up to 1200 °C for 60 µm, while 40 µm showed a slight grain growth in agreement with its enhanced recrystallization kinetics, and finally after achieving a nearly full recrystallization at 1200 °C (see also Fig. 4), both 40 and 60 µm exhibited a significant grain coarsening to around 110–120 µm by solution annealing at 1250 °C (Fig. 5).

Kernel average misorientation (KAM) maps and corresponding GND density distributions, for all samples are depicted in Figs. 6, and 7, respectively. It is evident that the GNDs density reduces by increasing the solution annealing temperature in line with KAM maps, as well as the low angle boundary fraction trends seen in Fig. 3. The GNDs density drops drastically for 40 µm (67 J/mm^3) already at 1150°C solution

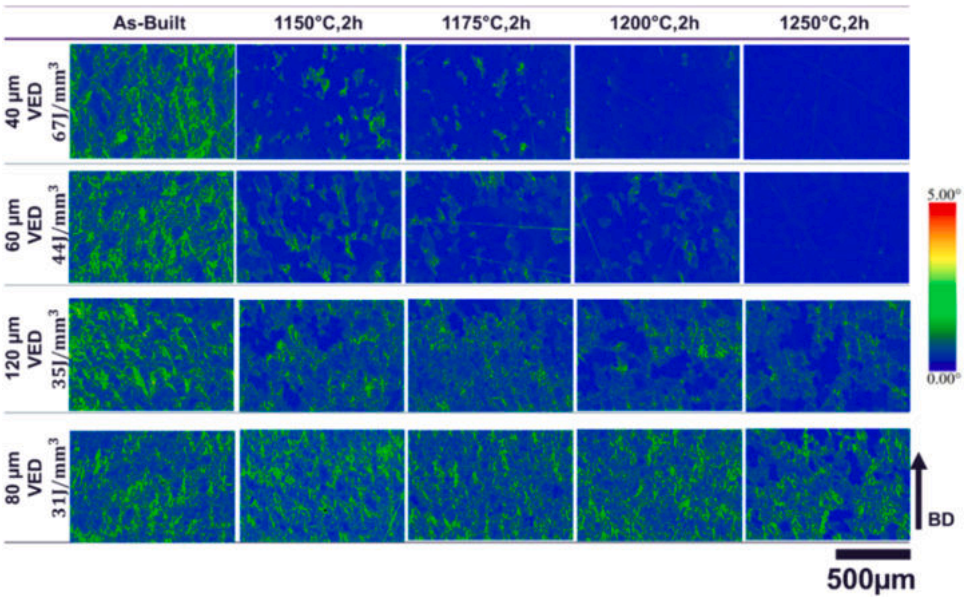

Fig. 6. KAM results for AB and solution annealed samples.

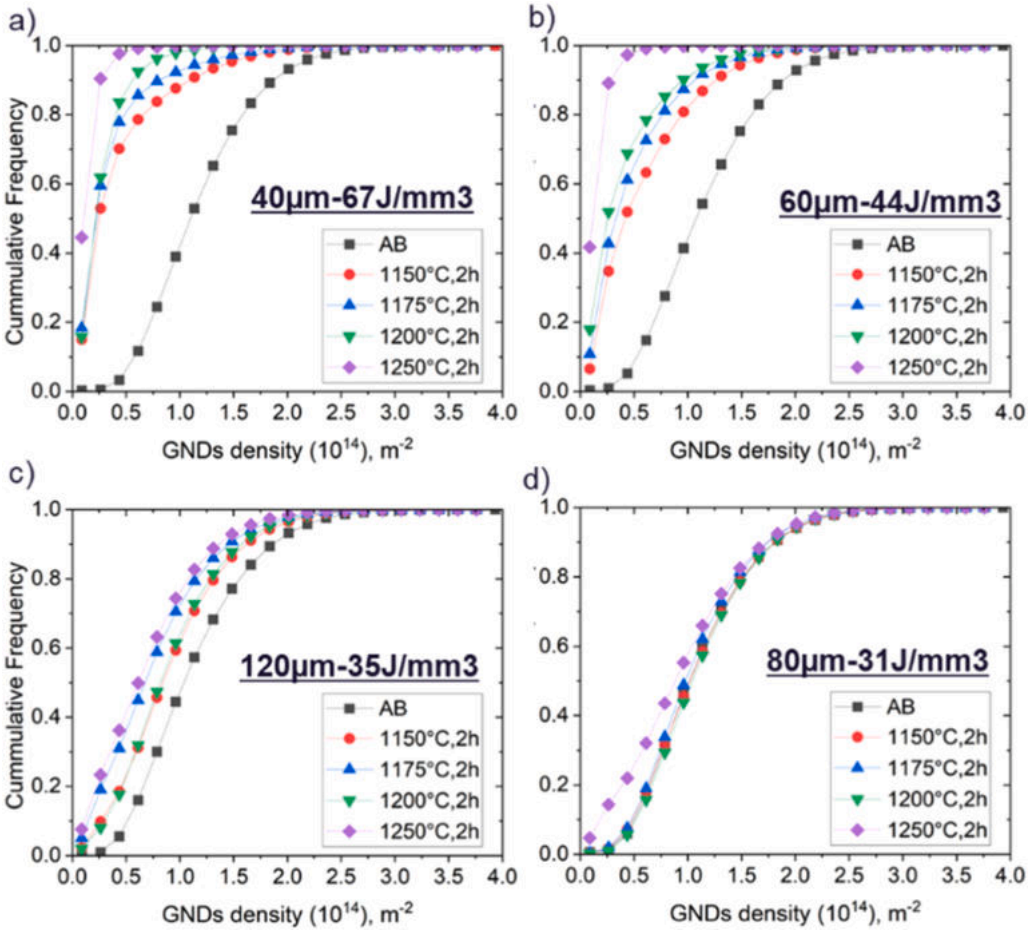

Fig. 7. GNDs density distributions calculated from KAM maps, considering a threshold of 2° misorientation, for AB and solution annealed samples: (a) 40 µm, (b) 60 µm, (c) 120 µm, and (d) 80 µm.

annealing (Fig. 7a), and the kinetics become gradually slower in 60 µm (44 J/mm^3), 120 µm (35 J/mm^3), and 80 µm (31 J/mm^3) samples (Fig. 7b-d), in-line with the previously discussed results in Fig. 4. Indeed, in 120 µm and 80 µm samples (Figs. 7c, and d), the dislocation density drops insignificantly even at the maximum solution annealing temperature of 1250°C, confirming their poor recrystallization behavior

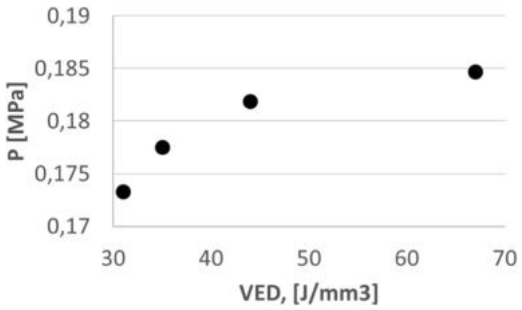

Fig. 8. Driving force for static recrystallization vs. VED.

(Fig. 4) as well as insignificant drop in hardness seen in Fig. 3.

Discussion

The average GNDs densities in AB condition were measured as 7.2×10^{13} /m^{2,} 7.0×10^{13} /m^2, 6.9×10^{13} /m^2, and 6.8×10^{13} /m^2 for 40 μm (67 J/mm^3), 60 μm (44 J/mm^3), 120 μm (35 J/mm^3), and 80 μm (31 J/mm^3), respectively. This agrees with the trend of lattice micro-strain and low angle boundary fractions, manifesting a larger dislocation density in samples processed by higher VEDs. However, it must be noted that EBSD scans were performed with a large step size of 2 μm, therefore, the resolution of the GNDs measurements can be quite low, as most of the dislocation density is known to be generated at the cell walls of L-PBF austenitic alloys, and the cell sizes are normally 200 nm to 1 μm [4,22,25]. In this single-phase austenitic material, the driving force for recrystallization increases by increasing dislocation density which scales with the energy stored (ΔE) in material [26]. In laser powder bed fusion, this stored energy is a result of the dramatic thermal strains due to the rapid cooling and subsequent heating and cooling cycles [25]. For the case of primary static recrystallization, the driving force (P) stems from the stored dislocations [27] (Eq. (2))

$$P = \rho E_{disl} = \frac{1}{2}\rho G b^2 \tag{2}$$

where E_{disl} is the elastic energy of a dislocation per line segment, ρ is the dislocation density, G is the shear modulus (82 GPa), and b the magnitude of the Burgers vector (0.25 nm) [28]. By entering the GNDs densities in Eq. (2), it is evident that the driving force for recrystallization increases by increasing the VED (Fig. 8). Therefore, in samples processed with a higher VED, the recrystallization kinetic is enhanced, because of higher stored energy, in view of lattice micro-strain and fraction of low angle boundaries (i.e., dislocation density), which was backed by the initial AB hardness, and yield strength (see Fig. 1).

It must be noted that using EBSD only GNDs densities could be quantified, and the numbers reported using Eq. (2) should be considered semi-quantitative as the values for statistically stored dislocations is missing. Therefore, to get a more physically meaningful confirmation on the effect of VED on the dislocation density, Eq. (3) can be used [29]. In this equation, the normalized stored energy of the lattice *(V)* scales with the mean square of micro-strain *(S^2)*, and E (Young's modulus) [29]. Unlike the EBSD analysis revealing only the geometrically necessary dislocations, the XRD data might account for statistically stored dislocations as well.

$$V = 3E\frac{S^2}{2} \tag{3}$$

Taking the L-PBF process heat input normalized by volume (i.e., VED) proportional to the stored energy of the lattice, there should be a linear relation between VED, and mean square of lattice micro-strain according to Eq. (3) (i.e., right side of the equation). This is shown and confirmed in Fig. 9a. Finally, a simplified process map, using the experimental data, is proposed to give an overview of the combined effect of laser energy and the heat treatment temperature on the recrystallization rate (Fig. 9b).

Conclusions

In summary, the recrystallization behavior of L-PBF processed HX, a single phase Ni superalloy, was studied. Particular emphasis was given to the influence of layer thickness and laser energy density on the recrystallization response. The following conclusions were made.

- The as built grain morphology and texture (// BD) was affected by the laser energy density where the samples processed with larger layer thicknesses, hence generally lower volumetric energy densities, showed a transition from the highly columnar and textured microstructure to equiaxed and less textured microstructures.
- Larger VEDs, led to larger stored energy in the form of dislocations, and enhanced recrystallization kinetics. Lower solution annealing temperature was required to achieve higher recrystallized fraction.
- Even if larger layer thicknesses could significantly improve the productivity in AM processes, the lower driving force for recrystallization, limits the effect of post heat treatment aimed at reducing anisotropy and achieving larger grain sizes. This must be taken into consideration especially for superalloys requiring high creep strength.

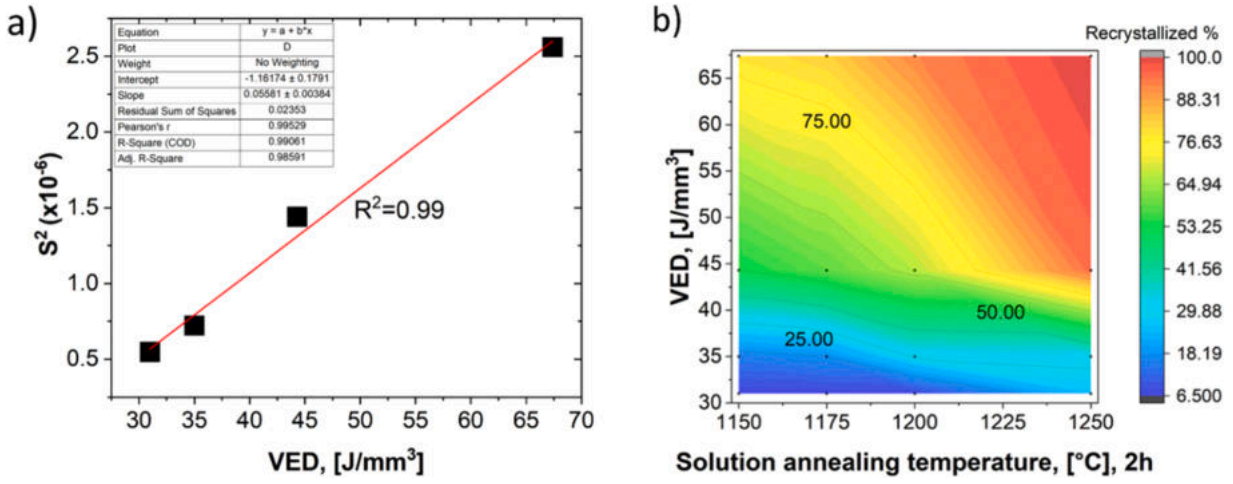

Fig. 9. (a) relation between VED, and square mean of lattice micro-strain, (b) a simplified map showing the dependence of recrystallization on VED, and temperature.

Declaration of Competing Interest

The authors declare that they have no known competing financial interests or personal relationships that could have appeared to influence the work reported in this paper.

Data availability

The data that has been used is confidential.

Supplementary materials

Supplementary material associated with this article can be found, in the online version, at doi:10.1016/j.addlet.2023.100182.

References

[1] M.L. Montero-Sistiaga, S. Pourbabak, J. Van Humbeeck, D. Schryvers, K. Vanmeensel, Microstructure and mechanical properties of Hastelloy X produced by HP-SLM (high power selective laser melting), Mater. Des. 165 (2019), 107598, https://doi.org/10.1016/j.matdes.2019.107598.

[2] H. Kirchhöfer, F. Schubert, H. Nickel, Precipitation behavior of Ni–Cr–22 Fe–18 Mo (Hastelloy-X) and Ni-Cr-22 Co-12 Mo (Inconel-617) after isothermal aging, Nucl. Technol. 66 (1984) 139–148, https://doi.org/10.13182/NT84-A33462.

[3] J.C. Zhao, M. Larsen, V. Ravikumar, Phase precipitation and time–temperature-transformation diagram of Hastelloy X, Mater. Sci. Eng. A 293 (2000) 112–119, https://doi.org/10.1016/S0921-5093(00)01049-2.

[4] F. Deirmina, S. Koenig, M. Hasselqvist, E. Oscarsson, O. Adegoke, N.H. Pettersson, M. Pellizzari, Influence of boron on the stress-rupture behavior of an additively manufactured Hastelloy X, Mater. Sci. Eng. A. 863 (2023), 144483, https://doi.org/10.1016/j.msea.2022.144483.

[5] S.T. McClain, D.R. Hanson, E. Cinnamon, J.C. Snyder, R.F. Kunz, K.A. Thole, Flow in a simulated turbine blade cooling channel with spatially varying roughness caused by additive manufacturing orientation, J. Turbomach. (2021) 143, https://doi.org/10.1115/1.4050389.

[6] O. Sanchez-Mata, J.A. Muñiz-Lerma, X. Wang, S.E. Atabay, M. Attarian Shandiz, M. Brochu, Microstructure and mechanical properties at room and elevated temperature of crack-free Hastelloy X fabricated by laser powder bed fusion, Mater. Sci. Eng. A 780 (2020), 139177, https://doi.org/10.1016/j.msea.2020.139177.

[7] Z. Huang, Z. Zhai, W. Lin, H. Chang, Y. Wu, R. Yang, Z. Zhang, On the orientation dependent microstructure and mechanical behavior of Hastelloy X superalloy fabricated by laser powder bed fusion, Mater. Sci. Eng. A 844 (2022), 143208, https://doi.org/10.1016/j.msea.2022.143208.

[8] X. Zhang, H. Xu, Z. Li, A. Dong, D. Du, L. Lei, G. Zhang, D. Wang, G. Zhu, B. Sun, Effect of the scanning strategy on microstructure and mechanical anisotropy of Hastelloy X superalloy produced by laser powder bed fusion, Mater. Charact. 173 (2021), 110951, https://doi.org/10.1016/j.matchar.2021.110951.

[9] Y. Yin, J. Zhang, J. Gao, Z. Zhang, Q. Han, Z. Zan, Laser powder bed fusion of Ni-based Hastelloy X superalloy: microstructure, anisotropic mechanical properties and strengthening mechanisms, Mater. Sci. Eng. A 827 (2021), 142076, https://doi.org/10.1016/j.msea.2021.142076.

[10] C. Li, Y. Liu, T. Shu, W. Guan, S. Wang, Effect of solution heat treatment on microstructure, mechanical and electrochemical properties of hastelloy X fabricated by laser powder bed fusion, J. Mater. Res. Technol. 24 (2023) 1499–1512, https://doi.org/10.1016/j.jmrt.2023.03.108.

[11] J. Kangazian, M. Shamanian, A. Kermanpur, F. Sadeghi, E. Foroozmehr, An investigation on the microstructure and compression properties of laser powder-bed fusion fabricated Hastelloy X Ni-based superalloy honeycomb structures, Mater. Sci. Eng. A 853 (2022), 143797, https://doi.org/10.1016/j.msea.2022.143797.

[12] A. Leicht, M. Fischer, U. Klement, L. Nyborg, E. Hryha, Increasing the productivity of laser powder bed fusion for stainless steel 316l through increased layer thickness, J. Mater. Eng. Perform. 30 (2021) 575–584, https://doi.org/10.1007/s11665-020-05334-3.

[13] A. Gullane, J.W. Murray, C.J. Hyde, S. Sankare, A. Evirgen, A.T. Clare, On the use of multiple layer thicknesses within laser powder bed fusion and the effect on mechanical properties, Mater. Des. 212 (2021), 110256, https://doi.org/10.1016/j.matdes.2021.110256.

[14] A. Cutolo, B. Neirinck, K. Lietaert, C. de Formanoir, B. Van Hooreweder, Influence of layer thickness and post-process treatments on the fatigue properties of CoCr scaffolds produced by laser powder bed fusion, Addit. Manuf. 23 (2018) 498–504, https://doi.org/10.1016/j.addma.2018.07.008.

[15] C. Schwerz, F. Schulz, E. Natesan, L. Nyborg, Increasing productivity of laser powder bed fusion manufactured Hastelloy X through modification of process parameters, J. Manuf. Process. 78 (2022) 231–241, https://doi.org/10.1016/j.jmapro.2022.04.013.

[16] M. Calcagnotto, D. Ponge, E. Demir, D. Raabe, Orientation gradients and geometrically necessary dislocations in ultrafine grained dual-phase steels studied by 2D and 3D EBSD, Mater. Sci. Eng. A. 527 (2010) 2738–2746, https://doi.org/10.1016/j.msea.2010.01.004.

[17] L. Lutterotti, S. Matthies, H.R. Wenk, A.S. Schultz Jr., J.W. Richardson, Combined texture and structure analysis of deformed limestone from time-of-flight neutron diffraction spectra, J. Appl. Phys. 81 (1997) 594–600, https://doi.org/10.1063/1.364220.

[18] J.O. Andersson, T. Helander, L. Höglund, P. Shi, B. Sundman, Thermo-Calc & DICTRA, computational tools for materials science, Calphad 26 (2002) 273–312, https://doi.org/10.1016/S0364-5916(02)00037-8.

[19] O. Gokcekaya, T. Ishimoto, S. Hibino, J. Yasutomi, T. Narushima, T. Nakano, Unique crystallographic texture formation in Inconel 718 by laser powder bed fusion and its effect on mechanical anisotropy, Acta Mater. 212 (2021), 116876, https://doi.org/10.1016/j.actamat.2021.116876.

[20] H.C. Hyer, C.M. Petrie, Effect of powder layer thickness on the microstructural development of additively manufactured SS316, J. Manuf. Process. 76 (2022) 666–674, https://doi.org/10.1016/j.jmapro.2022.02.047.

[21] S. Nath, P. Shukla, X. Shen, J. Lawrence, Effect of Laser Shock Peening (LSP) on the microstructure, residual stress state and hardness of a Nickel based Superalloy, in: 2017.

[22] H.E. Sabzi, N.T. Aboulkhair, X. Liang, X.H. Li, M. Simonelli, H. Fu, P.E.J. Rivera-Díaz-del-Castillo, Grain refinement in laser powder bed fusion: the influence of dynamic recrystallization and recovery, Mater. Des. 196 (2020), 109181, https://doi.org/10.1016/j.matdes.2020.109181.

[23] L. Monier, M. Buttard, M. Veron, J.J. Blandin, G. Martin, F. Villaret, Y. Shen, B. Yrieix, C. Ernould, J. Guyon, A. Despres, On the origin of grain refinement and twin boundaries in as-fabricated austenitic stainless steels produced by laser powder bed fusion, Addit. Manuf. 61 (2023), 103351, https://doi.org/10.1016/j.addma.2022.103351.

[24] F. Lin, Y. Zhang, A. Godfrey, D. Juul Jensen, Twinning during recrystallization and its correlation with the deformation microstructure, Scr. Mater. 219 (2022), 114852, https://doi.org/10.1016/j.scriptamat.2022.114852.

[25] F.C. Pinto, L.S. Aota, I.R. Souza Filho, D. Raabe, H.R.Z. Sandim, Recrystallization in non-conventional microstructures of 316L stainless steel produced via laser powder-bed fusion: effect of particle coarsening kinetics, J. Mater. Sci. 57 (2022) 9576–9598, https://doi.org/10.1007/s10853-021-06859-1.

[26] H.S. Zurob, Y. Bréchet, J. Dunlop, Quantitative criterion for recrystallization nucleation in single-phase alloys: prediction of critical strains and incubation times, Acta Mater. 54 (2006) 3983–3990, https://doi.org/10.1016/j.actamat.2006.04.028.

[27] D. Raabe, 23 - Recovery and recrystallization: phenomena, physics, models, simulation, Eds., in: D.E. Laughlin, K. Hono (Eds.), Physics of Metals and Metallography, Elsevier, Oxford, 2014, pp. 2291–2397, https://doi.org/10.1016/B978-0-444-53770-6.00023-X. Fifth Edpp

[28] A. Shaji Karapuzha, D. Fraser, D. Schliephake, S. Dietrich, Y. Zhu, X. Wu, A. Huang, Microstructure, mechanical behaviour and strengthening mechanisms in Hastelloy X manufactured by electron beam and laser beam powder bed fusion, J. Alloys Compd. 862 (2021), 158034, https://doi.org/10.1016/j.jallcom.2020.158034.

[29] G.K. Williamson, R.E. Smallman III, Dislocation densities in some annealed and cold-worked metals from measurements on the X-ray debye-scherrer spectrum, Philos. Mag. J. Theor. Exp. Appl. Phys. 1 (1956) 34–46, https://doi.org/10.1080/14786435608238074.